Acta Metall. Sin. (Engl. Lett.), 2016, **29**(9), 793–799
DOI 10.1007/s40195-016-0451-9

Corrosion Behavior of MgZnCa Bulk Amorphous Alloys Fabricated by Spark Plasma Sintering

Feng-Xiang Qin[1,2] · Chuan Ji[1] · Zhen-Hua Dan[2,3] · Guo-Qiang Xie[2] · Hao Wang[4] · Shin-Ichi Yamaura[2] · Mitsuo Niinomi[2] · Yang-De Li[5]

Received: 1 February 2016 / Revised: 8 June 2016 / Published online: 28 June 2016

Abstract Centimeter-sized $Mg_{65}Zn_{30}Ca_5$ bulk amorphous alloys were fabricated by the spark plasma sintering process from the amorphous powders with a size smaller than 5 μ m prepared by ball-milling. The sintered $Mg_{65}Zn_{30}Ca_5$ samples were in an amorphous state when the spark plasma sintering was performed at a temperature of 383 K under a pressure of 600 MPa. The data of polarization curves presented that the sintered $Mg_{65}Zn_{30}Ca_5$ bulk amorphous alloys exhibited higher corrosion resistance than pure Mg and AZ31B alloy owing to high content of Zn and homogeneous structure. A calcium phosphate compound layer was formed on the sintered $Mg_{65}Zn_{30}Ca_5$ bulk amorphous sample after immersion in Hanks' solution, which is effective in improving corrosion resistance and bioactivity. The sintered MgZnCa bulk amorphous alloys with large dimensions broaden the potential application of bulk amorphous alloys in the biomedical fields.

KEY WORDS: Mg; Bulk amorphous alloys; Spark plasma sintering; Corrosion behavior; Biomedical applications

1 Introduction

In recent years, magnesium and its alloys have attracted much interesting in application as biodegradable implant materials [1–7]. Mg ions have a natural presence in osseous tissue, and Mg is required for healthy skeletal development and maintenance. In comparison with other commercial biomedical alloys, such as Ti-based alloys, stainless steels and Co-based alloys, Mg-based alloys exhibit similar properties as the natural bones of humans, such as low density of 1.74 g/cm^3, proper strength and elastic modulus (41–45 GPa) [3, 4]. It is well known that Mg element is actively dissolved in the body fluids with a pH of about 7.4 [1–3]. Accordingly, the body fluids make the Mg implant dissolve and the second operation is avoided in clinic [2, 3]. Therefore, Mg alloys are new-generation biodegradable materials with high possibility. However, non-uniform corrosion behavior of Mg alloys shortens the lifetime and weakens the safety of the implants, i.e., the localized corrosion of crystalline Mg alloys limited their

Available online at http://link.springer.com/journal/40195

✉ Feng-Xiang Qin
fengxiangqin@njust.edu.cn

✉ Zhen-Hua Dan
zhenhuadan@njtech.edu.cn

[1] School of Materials Science and Engineering, Nanjing University of Science and Technology, Nanjing 210094, China

[2] Institute for Materials Research, Tohoku University, Sendai 980-8577, Japan

[3] College of Materials Science and Engineering, Nanjing TECH University, Nanjing 210009, China

[4] WPI-AIMR, Tohoku University, Sendai 980-8577, Japan

[5] Dongguan Eontech Co., Ltd, Dongguan 523662, China

biomedical application [3]. Mg-based amorphous alloys with homogeneous chemistry and structure are of great interest in biomedical applications due to their low Young's modulus, high strength, relative high corrosion resistance and good biocompatibility [3–6]. In comparison of Mg–RE–*M* amorphous alloys (RE: rare earth element; *M*: Ni, Cu, Zn), Mg–Zn–Ca amorphous alloys have been especially studied with reference to biosafety and biocompatibility [4–6]. The hydrogen evolution can be greatly reduced in Mg–Zn–Ca amorphous alloys and only marginal hydrogen evolution in vitro and in vivo degradation [5]. High cell viabilities and cell proliferation were also reported on the surface of Mg–Zn–Ca bulk amorphous alloys [3, 4].

Although Mg-based amorphous alloys exhibit many merits as biodegradable candidate materials, the limitations of the dimensional size and high degradation rate still restrict their applications. The maximum dimensions of Mg–Zn–Ca amorphous alloys prepared by rapid solidifications are limited in several millimeters and hardly meet the requirements of the implants in clinic [3–6]. Spark plasma sintering (SPS) process, as a developed rapid sintering technique, has a great potential for sintering bulk amorphous alloys with a larger dimensional size [8–10]. The SPS process is a type of solid-state compression sintering technique better than hot-pressing in case of crystallization of amorphous alloys in the sintering process, so that the sintered amorphous alloys with large sizes and complicated shapes can be easily produced. By using the SPS process, some bulk amorphous alloys and their composites have been fabricated [8–10]. The reports on Mg-based bulk amorphous alloys prepared by SPS technique are relatively rare [11]. As has been reported, ball-milling process can be employed to fabricate the Mg-based amorphous powders [11, 12], which can be sintered by SPS process.

In addition, the lifetime of Mg implant depends on the degradation rate, i.e., corrosion rate of the Mg-based alloys decides the lifetime of the implants. The lifetimes of Mg alloys are insufficient as an orthopedic biomaterial because the failure or disintegration occurs before the patient is cured since the Mg is so active in aqueous solution. Hence, improvement of the corrosion resistance and bioactivity of the biodegradable Mg-based amorphous alloy is necessary and imperative for the application of them. The corrosion resistance of Mg-based alloys can be improved by alloy designs and coating modifications [13–16]. Calcium phosphate compound coating is effective in increasing corrosion resistance of Mg alloys by separating Mg substrate from the solution because of low solubility of them [14, 15]. It is expected that the formation of calcium phosphate compound layer on Mg-based amorphous alloy may increase surface activity and decrease corrosion rate of Mg-based amorphous alloy [18]. Consequently, it is helpful to retard the degradation and enhance bioactivity of Mg–Zn–Ca amorphous alloys if calcium phosphate compound layer may form on the surface. In the present research, the ball-milling method was employed to fabricate amorphous powders from crystalline $Mg_{65}Zn_{30}Ca_5$ mother alloys, and then, bulk amorphous alloys with a centimeter size were fabricated by SPS technique. The corrosion behavior of sintered $Mg_{65}Zn_{30}Ca_5$ bulk amorphous alloy in Hanks' solution was investigated by the polarization measurements.

2 Experimental Procedure

A mixture of pure elements (>99.9 wt%) of Mg, Zn and Ca was melted in an induction furnace with the nominal compositions of $Mg_{65}Zn_{30}Ca_5$ (at.%). Ball-milling was performed under an inert argon atmosphere in a Retsch planetary ball mill (PM 100). The crystalline properties of the ball-milled powders were verified by X-ray diffraction (XRD) with Cu$K\alpha$ radiation. The amorphous powders were pre-compacted and then sintered in a vacuum chamber by a SPS system (Model SPS-3.20MK-IV). The heating rate was controlled at a speed of 26.7 K/min (from room temperature to T_s-30 K) and 5 K/min (T_s-30 K to T_s), where T_s is the sintering temperature. The holding time at the sintering temperature was 10 min. A uniaxial pressing method was conducted by using top and bottom WC hard metal punches with a loading pressure of 600 MPa. The sintered samples had a cylindrical shape with a diameter of 15 mm and a height of about 5 mm. A uniaxial compression testing was conducted with a conventional mechanical testing machine (Shimadzu, Autograph AG-X) at room temperature with an initial strain rate of 5×10^{-4} s^{-1}. The compression test samples with a rectangular shape in size of 2.5 mm × 2.5 mm × 5.0 mm were mechanically cut out from the sintered samples, and then, the surfaces were polished.

The samples used for the electrochemical testing with a rectangular shape of 2 mm in width, 2 mm in length and 4 mm in height were cut out from the sintered samples, and the samples were covered by resin. The sample surface was finished by 1000# grit SiC papers. Three samples or more for each condition were tested to get a reproducible result. Microstructures of the sintered samples were observed by a scanning electron microscopy (SEM, JEOL 6500). The corrosion behavior of the sintered samples was evaluated by potentiodynamic polarization measurement. Electrochemical evaluation was performed in Hanks' solution with pH 7.4 at 310 K open to air, which was prepared from the reagent grade chemicals and deionized water. The composition of Hanks' solutions (g/L) is 8.00 NaCl, 0.40

KCl, 0.35 $NaHCO_3$, 0.19 $CaCl_2{\cdot}2H_2O$, 0.09 $Na_2HPO_4{\cdot}7H_2O$, 0.2 $MgSO_4{\cdot}7H_2O$, 0.06 KH_2PO_4 and 1.00 glucose. Electrochemical measurements were taken in a three-electrode cell using a platinum counter electrode and an Ag/AgCl reference electrode. Potentiodynamic polarization curves were measured with a sweeping rate of 1 mV/s. High-purity Mg (>99.9%), commercial AZ31B (Mg–3Al–1Zn alloy) and melt-spun $Mg_{65}Zn_{30}Ca_5$ ribbons were also tested for comparison. The elemental analysis of the natural and oxide layers formed on $Mg_{65}Zn_{30}Ca_5$ alloys before and after immersion in Hanks' solution at 310 K was conducted by an X-ray photoelectron spectrometer (XPS, Shimadzu Kratos, AXIS-Ultra DLD) with monochromatized Al$K\alpha$ excitation ($h\gamma$ = 1486.6 eV).

3 Results and Discussion

Figure 1 shows the XRD patterns of $Mg_{65}Zn_{30}Ca_5$ powders after ball-milling for different time. XRD pattern of small blocks of the initial mother alloy includes several diffraction peaks indicating that the initial mother alloy is in crystalline state. With the increase in milling time to 35 h, only one sharp peak overlapping on one halo peak demonstrates that some part of the crystalline powders gradually transformed into an amorphous state. After the mother alloys were ball-milled for 45 and 55 h, only one halo peak exists, suggesting that the as-milled powders are mainly in an amorphous state. The $Mg_{65}Zn_{30}Ca_5$ powders ball-milled for 55 h have an irregular shape as presented in Fig. 2a. As shown in Fig. 2b, all the powders have a particle size less than 5 μm, and the distribution ratio of the powders with a size less than 2 μm was more than 80%.

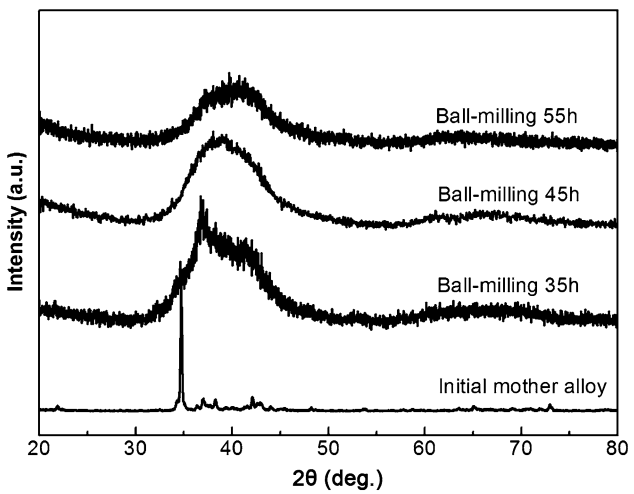

Fig. 1 XRD patterns of the ball-milled $Mg_{65}Zn_{30}Ca_5$ powders after different milling times. XRD pattern of the initial crystalline powders is also shown for comparison

Then, $Mg_{65}Zn_{30}Ca_5$ amorphous powders were sintered by the SPS process under a pressure of 600 MP with a holding time for 10 min at different sintering temperatures. The XRD patterns of the sintered samples are presented in Fig. 3. The XRD pattern of the sample sintered at 383 K shows a same broad halo peak in the range of 30°–45° as that of as-milled powder, meaning that the SPS process performed at 383 K has not changed the amorphous state of $Mg_{65}Zn_{30}Ca_5$ powders. The halo peak becomes sharper when the sintered temperature increases to 403 K. With further increasing the sintered temperature to 423 K, several diffraction peaks identified as Mg_7Zn_3 phase are observed. It indicates that the SPS process performed at a temperature higher than 403 K results in the crystallization of amorphous matrix and the Mg_7Zn_3 phase precipitates. The cross sections of the samples sintered at 383, 403 and 423 K were observed by SEM, as shown in Fig. 4. There exhibits no obvious contrast with crystalline phases, while some voids marked by white circles are observed which may act as beginning of cracking during the process of compression. The sintered $Mg_{65}Zn_{30}Ca_5$ sample exhibits strength of 450 MPa which is as high as commercial wrought Mg alloys. Although the compressive strength of sintered $Mg_{65}Zn_{30}Ca_5$ is lower than that of as-cast $Mg_{65}Zn_{30}Ca_5$, which was about over 700 MPa [14, 18], the strengths of sintered $Mg_{65}Zn_{30}Ca_5$ are still higher than that of commercial Mg alloys (200–400 MPa). Therefore, the strength of the examined alloys in this research is still satisfied with the requirement of absorbable stents or substantial bone.

Polarization curves of $Mg_{65}Zn_{30}Ca_5$ bulk amorphous alloy sintered at the temperature of 383 K are shown in Fig. 5. The data of high-purity Mg, commercial AZ31B alloy and $Mg_{65}Zn_{30}Ca_5$ melt-spun ribbon are also given for comparison. The corrosion potentials were confirmed to be about −1.60 V for pure Mg, −1.57 V for AZ31B alloy, −1.20 V for $Mg_{65}Zn_{30}Ca_5$ ribbons and −1.26 V for sintered $Mg_{65}Zn_{30}Ca_5$ bulk samples. The corrosion current densities were measured to be 1.3×10^{-6} A cm^{-2} for pure Mg, 4.1×10^{-6} A cm^{-2} for AZ31B alloys, 3.7×10^{-6} A cm^{-2} for $Mg_{65}Zn_{30}Ca_5$ ribbons and 3.8×10^{-6} A cm^{-2} for sintered bulk samples. The positive shift of the corrosion potential of sintered $Mg_{65}Zn_{30}Ca_5$ was more than 300 mV compared with pure Mg and AZ31B alloy. Usually, the conventional Mg alloys (such as AZ31, AZ41 and AZ91) corrode faster than high-purity Mg because of micro-coupling corrosion between alpha Mg matrix and second phases [19–23]. The sintered $Mg_{65}Zn_{30}Ca_5$ bulk samples exhibit similar corrosion properties as that of $Mg_{65}Zn_{30}Ca_5$ ribbon from the aspect of the corrosion potential and corrosion current density. The present Mg–Zn–Ca bulk amorphous alloys with a Zn content as high as 30% exhibit the characteristic of Zn

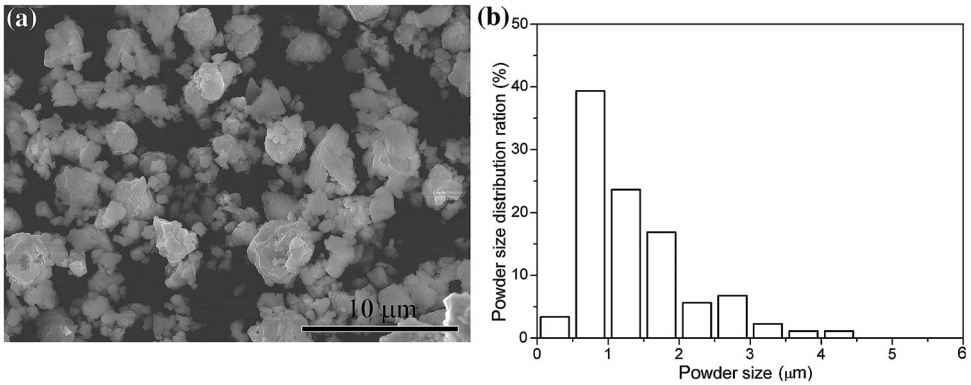

Fig. 2 SEM image **a** and powder size distribution ratio **b** of $Mg_{65}Zn_{30}Ca_5$ powders ball-milled for 55 h

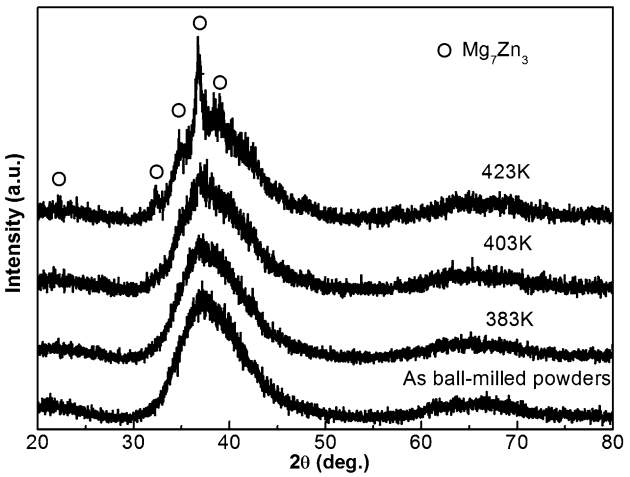

Fig. 3 XRD patterns of $Mg_{65}Zn_{30}Ca_5$ bulk amorphous alloys spark plasma sintered at various temperatures with a loading pressure of 600 MPa and holding time of 10 min

rather than that of Mg as conventional Mg alloys with low alloying elements, i.e., the high content of Zn element with high chemical stability is one reason that Mg–Zn–Ca bulk amorphous alloys exhibit much higher open-circuit potentials. Moreover, both composition and microstructure affect corrosion behavior of metallic materials in a certain solution. From the view of microstructure, $Mg_{65}Zn_{30}Ca_5$ bulk amorphous alloy is absent of the second phases, intermetallic phases and other defects. Chemically and structurally homogeneity of $Mg_{65}Zn_{30}Ca_5$ bulk amorphous alloy is another reason for the formation of a uniform oxide layer.

Elemental distribution and binding state of the surface oxide layers on sintered $Mg_{65}Zn_{30}Ca_5$ bulk samples before and after immersion in Hanks' solution for 72 h were analyzed by XPS. XPS wide-scan spectra of the samples exhibit peaks of O, C, Mg, Zn and Ca in both the native layer and oxide layer after immersion. C is the so-called contaminant carbon on the surface of the samples. It is worthy to note that P is also detected in the oxide layer after immersion in Hanks' solution. There is no obvious binding energy shift for Mg 1*s* peak in the native and oxide layers (Fig. 6a). From the previous research, it is known that the native layers of Mg-based amorphous alloys are mainly consisted of $Mg(OH)_2$, which can protect Mg from corrosion within the limitation of some extent [18]. The Zn 2*p* spectra in Fig. 6b are composed of two main peaks, which are identified as Zn $2p_{1/2}$ and Zn $2p_{3/2}$. In the native layer, Zn $2p_{1/2}$ and Zn $2p_{3/2}$ are located at about 1043.0 and 1019.9 eV, originating from metallic state. In the oxide layer after immersion in

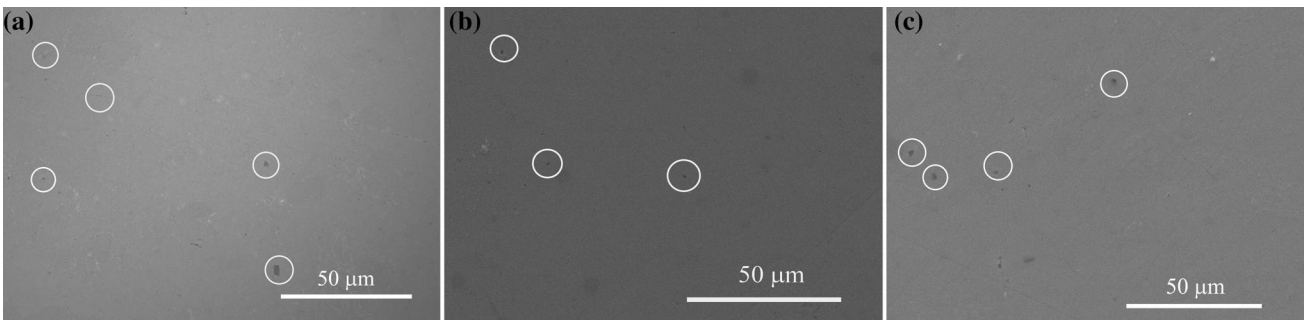

Fig. 4 SEM morphologies of $Mg_{65}Zn_{30}Ca_5$ bulk amorphous alloys sintered at 383 K **a**, 403 K **b**, 423 K **c**. The *white circles* mark the voids

Hanks' solution, binding energies of Zn $2p_{1/2}$ and Zn $2p_{3/2}$ shift to 1044.7 and 1021.5 eV, assigned as an oxidized species as Zn^{2+}. In the native layer, complicated Ca spectrum consists of five peaks by splitting of 2*p* plasmon, $2p^{2+}_{1/2}$, $2p^{0}_{1/2}$, $2p_{3/2}{}^{2+}$ and $2p^{0}_{3/2}$. In the oxide layer, Ca 2*p* peaks at 351.0 and 347.2 eV are assigned as the photoelectrons coming from the Ca^{2+}, as shown in Fig. 6c. From the results of the surface layer before and after immersion as shown in Fig. 6b, c, the main peaks shifted to higher binding energy after immersion, hinting that the Zn and Ca elements mainly existed in oxidized states in the form of Zn^{2+} and Ca^{2+}. As shown in Fig. 6d, the O 1*s* spectra are composed of three peaks at about 529.0, about 531.0 and ~533.0 eV in oxide layer, which were assigned as oxygen in OM, OH^- (phosphate) and H_2O, respectively. The OM oxygen is denoted the oxygen in metal–oxygen bonds, such as O^{2-} ions. P element exists in the form of phosphate in the oxide layer of the sintered $Mg_{65}Zn_{30}Ca_5$ bulk amorphous alloy after immersion, as presented in Fig. 6e, hinting the formation of phosphate compounds in the immersed surface. On the basis of the XPS data, it is known that the cations existing in the oxide layer were Mg^{2+}, Zn^{2+} and Ca^{2+}, and the anions were OH^- and $PO_4{}^{3-}$. There should be some calcium phosphate compound formed on the surface, or even more complicated phosphate salt with more than two kinds of cations and anions [17, 24].

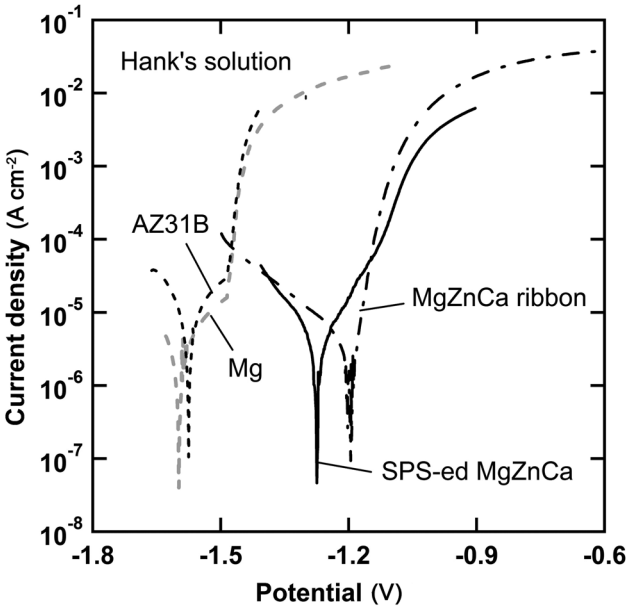

Fig. 5 Potentiodynamic polarization curves of $Mg_{65}Zn_{30}Ca_5$ bulk amorphous alloy fabricated by the SPS process at 383 K. The data of high-purity Mg, AZ31B alloy and $Mg_{65}Zn_{30}Ca_5$ amorphous ribbon are also shown for comparison

Figure 7 shows the relative concentration (defined as the ratio of the cationic fraction on the surface film to the designed bulk concentration) of the elements calculated from the integrated intensity of XPS on the native layer (before the immersion) and the oxide layer (after the

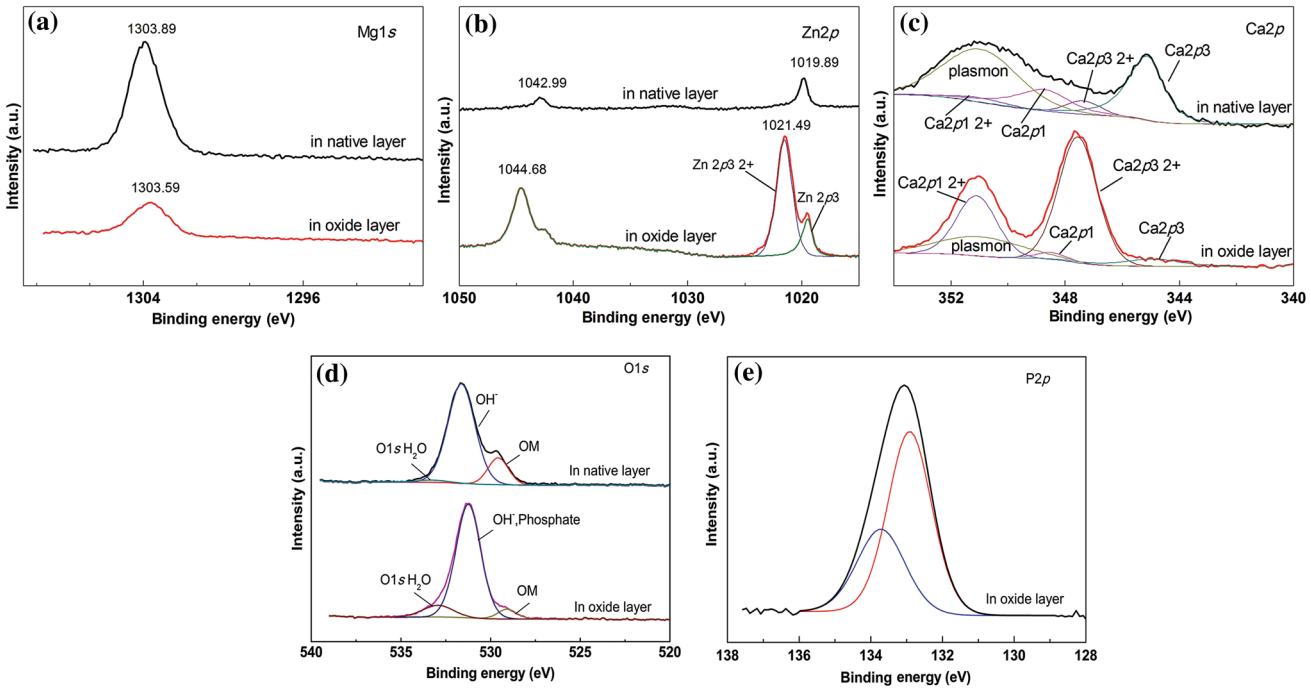

Fig. 6 XPS peaks of Mg 1*s* **a**, Zn 2*p* **b**, Ca 2*p* **c**, O 1*s* **d**, P 2*p* **e** in native layer (before immersion) and oxide layer (after immersion in Hanks' solution) of $Mg_{65}Zn_{30}Ca_5$ bulk amorphous alloys prepared by SPS

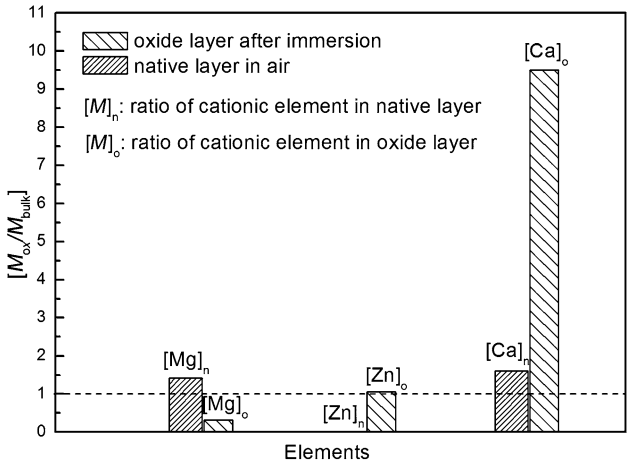

Fig. 7 Ratio of cationic element *M* (Mg, Zn, Ca) in the surface film to the $Mg_{65}Zn_{30}Ca_5$ bulk amorphous alloy ($[M_{ox}]/[M_{bulk}]$) after immersion in Hanks' solution

immersion) of the sintered amorphous samples. That is, the value of $[M_{ox}]/[M_{bulk}]$ corresponds to the enrichment or deficiency of the element $[M]$ on the surface film relative to the designed bulk composition, where $[M_{ox}]$ and $[M_{bulk}]$ denote the atomic concentration of element *M* in the surface layer and bulk alloy, respectively. The values higher and lower than unity mean enrichment and deficiency, respectively. Comparing the changes in the element fractions of the native layer and oxide layer, it is seen that the Ca concentration is much higher than that in bulk composition with the much decrease in Mg in the oxide layer after the immersion in Hanks' solution. In addition, the Zn content in oxide layer is same as that in the bulk alloys. In native layer, both Mg and Ca are enriched accompanying with the deficient of Zn element. The oxide layer formed on the sintered $Mg_{65}Zn_{30}Ca_5$ bulk amorphous alloy after immersion might consist of complex chemical compounds including small amount of $Mg(OH)_2$, $Zn_3(PO_4)_2$, and large amount of calcium phosphate compound. On the basis of the changes in the element fractions of the surface layers before and after immersion in Hanks' solution, it is known that the Zn concentration in the native layer is much lower than that in the substrate, compared with higher concentration of Ca and Mg because high affinity of Mg and Ca with oxygen makes them diffuse fast to the outer surface and causes a relative low concentration of Zn in the native layer. On the contrary, the concentration of these oxidized Ca and Zn compounds increased after immersion in Hanks' solution, whereas the concentrations of Mg are significantly deficient owing to active dissolution of $Mg(OH)_2$ during the process of immersion.

In the present work, centimeter-sized Mg–Zn–Ca bulk amorphous alloys have been fabricated by SPS process from the ball-milled amorphous powders. Relative high corrosion resistance was observed in Hanks' solution due to the formation of calcium phosphate compound layers. The $Mg(OH)_2$ formed in the native layer is actively dissolved accompanying with oxidization of Ca and Zn elements during serving in Hanks' solution since $Mg(OH)_2$ is in an active dissolution state in a solution with a pH lower than 12.4. The breakdown of the native $Mg(OH)_2$ layer is triggered by the aggressive attacks of Cl^- in the Hanks' solution with pH 7.4 [25, 26]. Calcium phosphate compound layer which forms during the immersion might contain Ca^{2+}, Zn^{2+}, and OH^- and PO_4^{3-} ions. On the basis of the change in the chemical composition of the oxide layer formed in Hanks' solution, the ratio between Ca^{2+} cation and PO_4^{3-} anions in the oxide layer on the sintered bulk amorphous sample is 1.44. And the ratio of (Ca+Zn)/P is 1.63, which is much close to the value 1.67 of Ca/P ratio in the apatite [24], hinting that Zn cations might partly substitute main cations to form a hydroxyapatite-like calcium phosphate compound with complex cations [17]. As reported, the solubility product of hydroxyapatite is 2.92×10^{-42}, which is much lower than those of $Zn(OH)_2$ ($K_{sp} = 1.8 \times 10^{-14}$) and $Mg(OH)_2$ ($K_{sp} = 5.1 \times 10^{-12}$) [17, 28]. These $Mg(OH)_2$, $Zn(OH)_2$ and Ca^{2+} sites in the native layer are considered to provide favorable sites for the hydroxyapatite-like calcium phosphate compound nucleation [27]. In the following, if those biomedical bulk amorphous alloys are applied as implants or artificial bones, the initial dissolution might be reduced dramatically since the initial dissolution of calcium phosphate compound/hydroxyapatite-like compound in Hanks' solution is very low as reported before [28, 29], and then, the lifetime of implanting will be enhanced in clinic. In addition, the formation of the hydroxyapatite-like calcium phosphate compound in the oxide layer is beneficial to enhancing the biocompatibility of sintered bulk amorphous alloys [5], while further research on the surface layer should be continued to confirm that the calcium phosphate layer formed on the surface of the Mg-based bulk amorphous alloy is hydroxyapatite or not, how the thickness of them affects the degradation rate.

4 Conclusions

The centimeter-sized $Mg_{65}Zn_{30}Ca_5$ bulk amorphous alloys were sintered by using a spark plasma sintering process from ball-milled amorphous powders. Higher corrosion resistance of sintered Mg–Zn–Ca bulk amorphous alloys than pure Mg and commercial AZ31B alloy was obtained in Hanks' solution in the view of positive open-circuit potential and lower corrosion current density. The surface layer of the sintered Mg–Zn–Ca bulk amorphous alloy after serving in Hanks' solution was mainly composed of

calcium phosphate compound, which may decrease the solubility and increase the biocompatibility. The sintered Mg–Zn–Ca bulk amorphous alloys open the possibilities of the applications of them as biodegradable materials offering excellent properties to meet large-size requirements.

Acknowledgments This work is financially supported by the Natural Science Foundation of China under Grant No. 51301091, the Natural Science Foundation of Jiangsu Province Grant No. BK20151536, the Fundamental Research Funds for the Central Universities No. AE16001 and the Advanced Materials Development and Integration of Novel Structured Metallic and Inorganic Materials from the Ministry of Education, Sport, Culture, Science and Technology, Japan.

References

[1] M.B. Kannan, R.K.S. Raman, Biomaterials **29**, 2306 (2008)
[2] F. Witte, J. Fischer, J. Nellesen, H. Crostack, V. Kaese, A. Pischd, F. Beckmann, H. Windhagen, Biomaterials **27**, 1013 (2006)
[3] Z. Li, X. Gu, S. Lou, Y. Zheng, Biomaterials **29**, 1329 (2008)
[4] X.N. Gu, Y.F. Zheng, S.P. Zhong, T.F. Xi, J.Q. Wang, W.H. Wang, Biomaterials **31**, 1093 (2010)
[5] B. Zberg, P.J. Uggowitzer, J.F. Löffler, Nat. Mater. **8**, 887 (2009)
[6] H. Li, S. Pang, Y. Liu, L. Sun, P.K. Liaw, T. Zhang, Mater. Des. **67**, 9 (2015)
[7] Y.C. Zhao, G.S. Huang, G.G. Wang, T.Z. Han, F.S. Pan, Acta Metall. Sin. (Engl. Lett.) **28**, 1387 (2015)
[8] G.Q. Xie, D.V. Louzguie-Luzgin, H. Kimura, A. Inoue, Appl. Phys. Lett. **2**, 121907 (2008)
[9] G.Q. Xie, D.V. Louzguie-Luzgin, H. Kimura, A. Inoue, Mater. Trans. **8**, 158 (2007)
[10] G.Q. Xie, D.V. Louzguie-Luzgin, H. Kimura, H. Men, A. Inoue, Intermetallics **20**, 76 (2012)
[11] F.O. Mèar, G.Q. Xie, D.V. Louzguine-Luzgin, A. Inoue, Mater. Trans. **50**, 588 (2009)
[12] J.Q. Wang, Y.H. Liu, M.W. Chen, D.V. Louzguine-Luzgin, A. Inoue, J.H. Perepezko, Sci. Rep. **2**, 418 (2012)
[13] F. Wang, J.B. Li, J. Liu, Acta Metall. Sin. (Engl. Lett.) **27**, 609 (2014)
[14] J. Li, H. Pei, W. Ji, S. Yang, S. Zhang, Y. Chen, C. Zhao, Z. Fan, X. Zhang, Y. Jiang, Mater. Sci. Eng. B **176**, 1785 (2011)
[15] X. Lin, X. Wang, L.L. Tan, P. Wan, X.M. Yu, Q. Li, K. Yang, Ceram. Int. **40**, 10043 (2014)
[16] R.C. Zeng, L.J. Liu, T.T. Pang, F. Zhang, W.W. Zhang, S.Q. Li, H.Z. Cui, E.H. Han, Acta Metall. Sin. (Engl. Lett.) **28**, 373 (2015)
[17] C.W. Robert (ed.), *Handbook of Chemistry Physics*, 66th edn. (CRC, Cleveland, 1985)
[18] F.X. Qin, G.Q. Xie, Z.H. Dan, S.L. Zhu, I. Seiki, Intermetallics **42**, 9 (2013)
[19] N. Hara, Y. Kobayashi, D. Kagaya, N. Akao, Corros. Sci. **49**, 166 (2007)
[20] N. Abidin, A.D. Atrens, D. Martin, A. Atrens, Corros. Sci. **53**, 3542 (2011)
[21] G. Song, A. Atrens, Adv. Eng. Mater. **5**, 837 (2003)
[22] Z. Shi, J.X. Jia, A. Atrens, Corros. Sci. **60**, 296 (2012)
[23] A. Atrens, M. Liu, N.I.Z. Abidin, Mater. Sci. Eng. B **176**, 1609 (2011)
[24] L.K. Sha, B.W. Chappell, Geochim. Cosmochim. Acta **63**, 3861 (1999)
[25] M. Pourbaix, *Atlas of Electrochemical Equilibria in Aqueous Solutions* (Pergamon Press, Oxford, 1966), pp. 139–145
[26] G.A. Parks, Chem. Rev. **65**, 177 (1965)
[27] T. Kokubo, Thermochim. Acta **280/281**, 479 (1996)
[28] M.T. Fulmer, I.C. Ison, C.R. Hankermayer, B.R. Constantz, J. Ross, Biomaterials **23**, 751 (2002)
[29] Y. Song, S. Zhang, J. Li, C. Zhao, Acta Biomater. **6**, 1736 (2010)